Journal of Geophysical Research: Space Physics

RESEARCH ARTICLE
10.1002/2017JA025099

Key Points:
- Shock-induced compression significantly alters the high-latitude convection patterns
- Large convection speed between PI and MI FACs caused significant frictional heating and subsequent heat transfer between ions and neutrals
- The simulation results in general reproduce observations despite lower magnitudes

Supporting Information:
- Supporting Information S1
- Movie S1
- Movie S2

Correspondence to:
D. S. Ozturk,
dcsoztrk@umich.edu

Citation:
Ozturk, D. S., Zou, S., Ridley, A. J., & Slavin, J. A. (2018). Modeling study of the geospace system response to the solar wind dynamic pressure enhancement on 17 March 2015. *Journal of Geophysical Research: Space Physics*, *123*, 2974–2989. https://doi.org/10.1002/2017JA025099

Received 5 DEC 2017
Accepted 16 MAR 2018
Accepted article online 23 MAR 2018
Published online 6 APR 2018

Modeling Study of the Geospace System Response to the Solar Wind Dynamic Pressure Enhancement on 17 March 2015

D. S. Ozturk[1], S. Zou[1], A. J. Ridley[1], and J. A. Slavin[1]

[1]Climate and Space Science and Engineering, University of Michigan, Ann Arbor, MI, USA

Abstract The global magnetosphere-ionosphere-thermosphere system is intrinsically coupled and susceptible to external drivers such as solar wind dynamic pressure enhancements. In order to understand the large-scale dynamic processes in the magnetosphere-ionosphere-thermosphere system due to the compression from the solar wind, the 17 March 2015 sudden commencement was studied in detail using global numerical models. This storm was one of the most geoeffective events of the solar cycle 24 with a minimum *Dst* of −222 nT. The Wind spacecraft recorded a 10-nPa increment in the solar wind dynamic pressure, while the interplanetary magnetic field B_Z became further northward. The University of Michigan Block-Adaptive-Tree Solar wind Roe-type Upwind Scheme global magnetohydrodynamic code was utilized to study the generation and propagation of perturbations associated with the compression of the magnetosphere system. In addition, the high-resolution electric potential and auroral power output from the magnetohydrodynamic model was used to drive the global ionosphere-thermosphere model to investigate the ionosphere-thermosphere system response to pressure enhancement. During the compression, the electric potentials and convection patterns in the polar ionosphere were significantly altered when the preliminary impulse and main impulse field-aligned currents moved from dayside to nightside. As a result of enhanced frictional heating, plasma and neutral temperatures increased at the locations where the flow speeds were enhanced, whereas the electron density dropped at these locations. In particular, the region between the preliminary impulse and main impulse field-aligned currents experienced the most significant heating with 1000-K ion temperature increase and 20-K neutral temperature increase within 2 min. Comparison of the simulation results with the Poker Flat Incoherent Scatter Radar observations showed reasonable agreements despite underestimated magnitudes.

Plain Language Summary During 17 March 2015, near-Earth environment was significantly perturbed due to an interplanetary shock. Using numerical models, we studied the effect of this shock on the geospace system. We have found that the compression due to the shock can affect the Earth's upper atmosphere immediately. The shock created various perturbations including but not limited to temperature and density variations, at low-Earth orbit altitudes, which are very important for spacecraft operations. Ground-based measurements supported our findings and revealed that the perturbations occurring were even more drastic than we modeled.

1. Introduction

Discontinuities and interplanetary shocks in the solar wind compress the Earth's magnetosphere and result in a global configuration change referred to as a sudden impulse (Smith et al., 1986). Traditionally studied with ground magnetometers, the sudden impulse signatures consist of two distinct magnetic perturbations at high latitudes with opposite polarities, a short-lived preliminary impulse (PI) followed by a longer lasting main impulse (MI; Araki, 1977). Various studies showed that the magnetospheric sources for the PI and MI magnetic perturbation signatures are different and the ionospheric sources for those perturbations are created by oppositely oriented field-aligned currents (FACs; Fujita, Tanaka, Kikuchi, Fujimoto, & Itonaga, 2003). The PI signature is thought to originate with the transverse Alfvén waves (Chi et al., 2001; Fujita, Tanaka, Kikuchi, Fujimoto, Hosokawa, et al., 2003; Nishida, 1964; Tamao, 1964) that are caused by magnetopause deformation (Kivelson & Southwood, 1991; Russell & Ginskey, 1995; Samsonov et al., 2011). On the other hand, the FACs that give rise to the MI signatures map inside of the magnetosphere, specifically to vortex-like structures that propagate from dayside to nightside (Fujita, Tanaka, Kikuchi, Fujimoto, & Itonaga, 2003; Kataoka, Fukunishi, & Lanzerotti, 2003; Ozturk et al., 2017; Slinker, Fedder, Hughes, et al., 1999; Yu & Ridley, 2011).

The generation of magnetospheric sources has been widely studied through theory and observations. Kivelson and Southwood (1991) was first to suggest that a rise in solar wind pressure may excite a pair of vortices with opposite senses of rotation in the dawn and dusk magnetosphere, which in turn creates a pair of transient FACs that resembles the MI FACs (Tanaka, 2007). This FAC pair transfers electromagnetic energy from the magnetosphere to the ionosphere (Tanaka, 2003, 2007). The excitation of oppositely oriented FAC pairs that results in PI and MI signatures has been shown in various global modeling studies (Fujita, Tanaka, Kikuchi, Fujimoto, & Itonaga, 2003; Fujita, Tanaka, Kikuchi, Fujimoto, Hosokawa, et al., 2003; Kataoka et al., 2004; Motoba et al., 2003; Ozturk et al., 2017; Samsonov & Sibeck, 2013; Yu & Ridley, 2011; Zhao et al., 2015).

Reconstruction of equivalent ionospheric currents from observed magnetic perturbations at ground magnetometers also revealed the configuration of the FACs and ionospheric horizontal currents (Hall and Pedersen currents; Kamide et al., 1976; Matsushita & Xu, 1982; Untiedt & Baumjohann, 1993; Weygand et al., 2011, 2012). The major contribution to the ground magnetic perturbations comes from the Hall currents under the assumption of a uniformly conducting ionosphere (Fukushima, 1969). Therefore, the equivalent ionospheric currents are a close approximation of the configuration of Hall currents (Keiling et al., 2009). Fukushima (1969) showed that the ionospheric flow patterns are antiparallel to the Hall currents. These convection flow profiles change significantly under sudden dynamic pressure enhancements forming traveling convection vortices (TCVs; Clauer et al., 1984; Friis-Christensen et al., 1988; Glassmeier & Heppner, 1992; Hönisch & Glassmeier, 1986; Lanzerotti et al., 1991). The TCVs are pairs of twin vortices that form on the dayside and propagate toward the nightside, together with the PI and MI FAC profiles, as shown in Yu and Ridley (2009), Fujita, Tanaka, Kikuchi, Fujimoto, and Itonaga (2003), and Ozturk et al. (2017). Some theoretical and observational studies have also found the links between the TCVs to the twin magnetospheric vortices in the equatorial plane (Glassmeier & Heppner, 1992; Glassmeier, Hönisch, & Untiedt, 1989; Keiling et al., 2009; Kim et al., 2015; Slinker, Fedder, Hughes, et al., 1999).

The formation and propagation of perturbation FACs significantly alter the background ionospheric convection. Even though the connection between magnetospheric perturbations and ionospheric convection has been studied extensively, the effects of perturbation FACs on the ionosphere-thermosphere (I-T) system are still not well understood. Pioneering work in understanding the local effects of FACs on the ionosphere system was conducted by Schunk et al. (1994). They used the Utah State University time-dependent ionospheric model to introduce a pair of oppositely directed FACs that propagate from dayside to nightside with a speed similar to that of TCV observations, 3 km/s. This study showed that the local NO^+ density and ion and electron temperatures are enhanced during the TCV passage, while the electron density and O^+ density are depleted.

The global I-T response to perturbations related to solar wind dynamic pressure enhancement has been studied with various observations (Kim et al., 2017; Valladares et al., 1999; Zou et al., 2017). Using the Greenland magnetometer arrays and the Sondrestrom and Super Dual Auroral Radar Network radars, Valladares et al. (1999) showed that ground magnetic perturbations larger than 100 nT are associated with elevated ion temperatures and plasma density depletions. Similarly, using the Poker Flat Incoherent Scatter Radar (PFISR), Zou et al. (2017) showed the ion temperatures increase drastically during the transition from the PI phase to the MI phase together with a persistent electron temperature increase and an ensuing density drop in the *F* region. Kim et al. (2017) used the Super Dual Auroral Radar Network and ground magnetometers to infer the pressure-induced ionospheric vortical convection patterns and also used the European Incoherent Scatter Svalbard Radar measurements to display electron and ion temperature enhancements and the Scanning Doppler Imager to demonstrate the variation in thermospheric winds. Oliveira et al. (2017) conducted a superposed epoch analysis of storm time neutral mass densities measured using the Challenging Minisatellite Payload and Gravity Recovery and Climate Experiment satellites. They showed that the thermosphere response to solar wind dynamic pressure enhancement was immediate. Similarly, Shi et al. (2017) reported enhanced neutral mass density measurements from the Challenging Minisatellite Payload and the Gravity Recovery and Climate Experiment satellites and also enhanced Poynting flux measurements from the Defense Meteorological Satellite Program during increased dynamic pressure intervals. In addition, using OpenGGCM model they showed that the location of enhanced Poynting Flux coincided with the new FAC systems that formed due to compression. The aforementioned studies showed that the pressure enhancement not only can strongly alter the local profiles in the ionosphere system but also has far-reaching

effects that are persistent even after the convection profile subsides. In this study, we further investigated the ionosphere and thermosphere responses to dynamic pressure enhancement induced PI and MI FACs.

Joule heating is a key parameter describing the momentum and energy transferred from the magnetosphere to the I-T (Knipp et al., 2004). Quantifying Joule heating through observations is very difficult due to the sparseness of continuous high-resolution measurements of ionospheric electric fields, electron density, and neutral winds (Deng & Ridley, 2007; Thayer, 1998; Verkhoglyadova et al., 2016). The numerical modeling of Joule heating is also arduous because most of the I-T models use empirical models that spatially and temporally smooth the electric field data (Codrescu et al., 1995; Foster et al., 1986; Heelis et al., 1982; Richmond et al., 1992; Thayer, 1998; Weimer, 1996). The loss of resolution due to the smoothing of the electric field combined with the lack of a precise conductivity model results in systematically underestimated values for Joule heating in numerical models (Deng & Ridley, 2007; Huang et al., 2016; Johnson & Heelis, 2005; Verkhoglyadova et al., 2016). Furthermore, most empirical models are steady state, implying that they do not accurately capture the dynamics during periods such as when the solar wind dynamic pressure increases. Therefore, employing electrodynamic solutions obtained from high temporal and spatial resolution physics-based global magnetosphere (GM) models to drive the I-T models has the potential to greatly improve the current understanding of geospace system response to solar wind dynamic pressure enhancement events. In this paper, we report a detailed study of the 17 March 2015 event, one of the most geoeffective events of solar cycle 24 (Kataoka et al., 2015; Wang et al., 2016). Its effects on the ionosphere have been studied widely (Cherniak et al., 2015; Fagundes et al., 2016; Jacobsen & Andalsvik, 2016; Liu et al., 2016; Verkhoglyadova et al., 2016) and was described in Zou et al. (2017), because the PFISR was at an ideal location to capture the propagation of shock-induced FAC and convection vortices. A self-consistent global magnetohydrodynamic (MHD) model was used in Zou et al. (2017) to reveal the global FAC and convection patterns. In this study, results from the same MHD model were used to drive a global I-T model to investigate the I-T system responses to solar wind dynamic pressure enhancement. By using the high-resolution electric field potential and auroral precipitation output from the global MHD model, we explored the detailed transient momentum and energy transfer from the magnetosphere to the upper atmosphere.

2. Methodology

2.1. Simulation Setup

To accurately represent the solar wind interaction with the magnetosphere-ionosphere system, we used the GM, inner magnetosphere (IM), and ionospheric electrodynamics (IE) modules of the Space Weather Modeling Framework (SWMF) (Toth et al., 2005). The global MHD code Block-Adaptive-Tree Solar wind Roe-type Upwind Scheme (BATS-R-US) was used in the GM region to solve for the ideal MHD equations and was coupled with the IM and IE components (Powell et al., 1999; Tóth et al., 2012; Ridley et al., 2016). The IE component was the Ridley Ionosphere Model (RIM; Ridley et al., 2004), which was driven by the FACs and auroral power computed from the GM component and estimated the ionospheric electric potential based on FACs and conductance. The potential solution was then mapped out to the GM inner boundary at 2.5*Re* where it was used to drive the motion of the magnetic field lines in BATS-R-US. We used the Comprehensive Ring Current Model (Fok et al., 2001; Glocer et al., 2013) to represent the IM component, which was two-way coupled with the GM component and received the ionospheric electric potential solution from IE.

The BATS-R-US MHD simulation was driven by the solar wind and interplanetary magnetic field (IMF) data obtained from the Wind spacecraft at L1, propagated to the upstream boundary at $X = 32Re$. To minimize the timing uncertainties associated with the propagation, we shifted the simulation results by 16 min to match the observed compression time in the Sym-H index. The IMF B_Y, B_Z, X component of the solar wind velocity in geocentric solar magnetospheric coordinates, and number density obtained from the Wind spacecraft, as well as the Sym-H index, are shown in Figure 1a. The B_Y, B_Z, V_X, number density, and solar wind dynamic pressure values taken at the dayside subsolar point from the simulation are shown in Figure 1b for comparison. The Sym-H index shown in Figure 1a indicates that the compression occurred at 0445 UT. Both velocity and density shown in Figure 1a are flat before the compression, whereas in Figure 1b, both values show a mild enhancement at 0442 UT, that is, ~50 km/s in velocity and ~3 cm^{-3} in density, respectively. This compression signals in the upstream conditions may sometimes occur in numerical simulations,

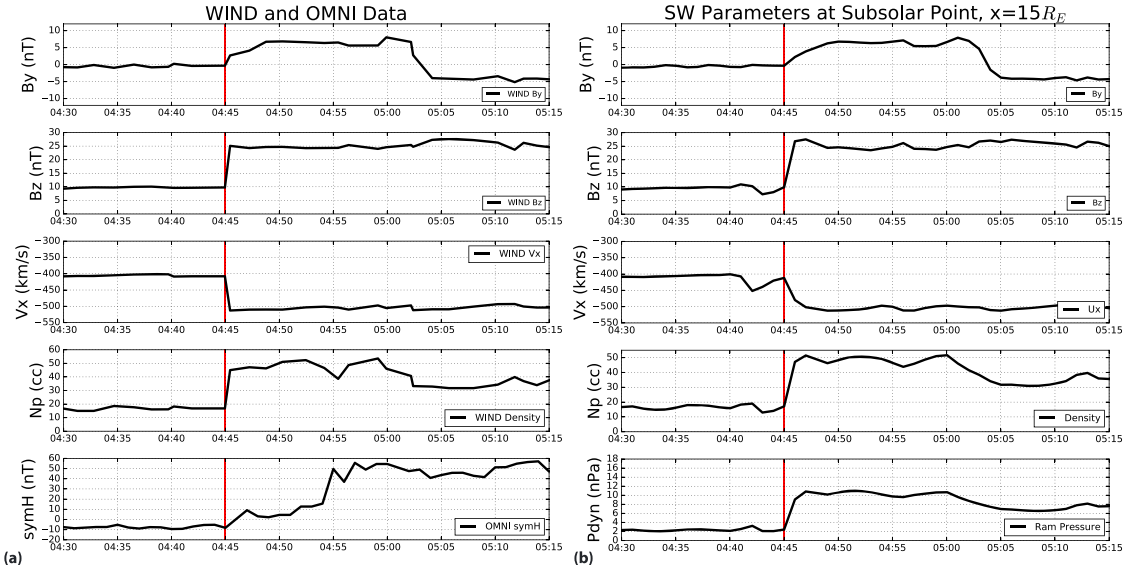

Figure 1. The interplanetary magnetic field and solar wind parameters obtained from the Wind spacecraft through CDAWeb and the Sym-H index obtained from OMNIWeb are shown on the left bottom panel (a). The solar wind parameters taken from the simulation at the subsolar point at $X = 15Re$ are shown on the right (b). The red line shows the start of event detected by the ground magnetometers.

because the MHD solvers allow for small amounts of divergence B to occur, which is then stabilized with waves generated close to discontinuities (Powell, 1994; Toth, 2000). Besides this minor compression, the upstream solar wind properties extracted at subsolar point, shown in Figure 1b, closely resembled the WIND observations shown in Figure 1a. At 0445 UT, V_X increased from 420 to 510 km/s, whereas the density increased from 18 to 58 cm^{-3} at 15*Re*, just upstream of the bow shock. Prior to the event, the IMF B_Y was close to zero, which indicates that there was most likely a symmetric configuration of the ionospheric FACs. However, with the start of the compression, the IMF B_Y became positive and stayed positive until 0504 UT. This variation in the IMF B_Y is expected to create a dawn-dusk asymmetry in the FACs (Tanaka, 2001). The IMF B_Z was around 10 nT before the compression and became further northward exceeding 25 nT, afterward.

For this study, the GM inner boundary was set to 2.5*Re* from the center of the Earth. The computational domain was a three-dimensional box in geocentric solar magnetospheric coordinates that started from 32*Re* upstream of the Earth in the *X* direction to 224*Re* tailward and −128*Re* to +128*Re* both in the *Y* and *Z* directions. The finest resolution was closest to Earth, where the cells had 1/8 *Re* grid resolution. To understand the global magnetic signatures on the ground, we implemented 600 virtual ground magnetometers in each hemisphere uniformly from the magnetic equator up to 80° latitude (4° in latitude by 12° in longitude).

The results obtained from the coupled GM-IM-IE modules including convection and auroral precipitation were used to drive the global ionosphere-thermosphere model (GITM; Ridley et al., 2006). The GITM is a three-dimensional, parallel, spherical code that uses a stretched altitude grid and allows nonhydrostatic solutions. The model self-consistently solves the electron, major ion, and neutral temperatures, densities, and velocities (Zhu & Ridley, 2016). For this study, we used a spatial resolution of 4° in longitude to 1° in latitude for the region between ~100 and ~600 km. The GITM simulation was first driven by the empirical Weimer convection model (2005) and the Ovation aurora model (Newell et al., 2002), from 15 March 2015 0000 UT, that is, 2 days before the event, to 17 March 2015 0405 UT, that is, ~40 min before the compression, in order to allow the model to converge to a solution that was not influenced by the initial condition. These empirical models were run with the Wind measurements of solar wind and IMF as inputs. From 0405 UT onward, we used the electric potentials and auroral precipitation obtained from the MHD simulation to drive the GITM, updating the electrodynamic patterns every 10 s to better capture the temporal and spatial variations associated with the solar wind drivers.

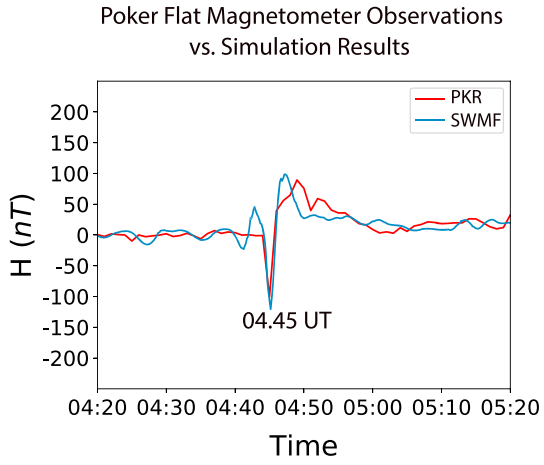

Figure 2. The comparison of the magnetic field *H* component measured by the Poker Flat magnetometer (red) and modeled by the virtual magnetometer at the same location (blue). The negative preliminary impulse signature associated with compression was observed at 0445 UT (adapted from Figure 5 in Zou et al., 2017).

2.2. Validation of the Simulation Results

In order to validate the model, we also included virtual magnetometers at the same locations as the real ground magnetometers. A comparison of the Poker Flat (PKR) magnetometer observation of the *H* component perturbations, and the virtual magnetometer is shown at the same location and can be seen in Figure 2 (adapted from Figure 5 in Zou et al., 2017). After the baseline was extracted, the PKR magnetometer recorded a sharp decrease of ~120 nT starting at 0445 UT, which was the PI signature associated with the real compression. The PI dip was then followed by a positive perturbation of ~100 nT that corresponded to the MI signature of the compression. The virtual magnetometer responded to the minor numerical compression shown in Figure 1b at 0442 UT. The good agreement between the MHD model results and the PKR observations indicated that the BATS-R-US MHD model captured the EI well at this location and could be used to drive the GITM to further investigate the I-T responses here.

3. Results

The simulation results obtained from the Space Weather Modeling Framework and the GITM are shown in this section. The first subsection focuses on the magnetospheric and ionospheric responses from the Space Weather Modeling Framework. The equatorial flow profiles at the magnetosphere and the traced magnetic field lines that link the perturbations in the flow to the top of the ionosphere are shown in section 3.1. The evolutions of FACs, the simplified Joule Heating derived from the RIM on top of the ionosphere, ion temperature and convection at 227 km, and horizontal (*H*) component of the magnetic perturbations recorded by virtual magnetometers before, during, and after the compression are discussed in section 3.2. The section follows with a discussion of the response of the ionospheric and thermospheric variations at two distinct locations to highlight the dawn-dusk asymmetry and compares the simulation results with the PFISR observations.

3.1. Magnetospheric Response

The magnetospheric response to the compression is shown in Figure 3 for two time steps, that is, the beginning of the PI phase at 0445 UT and 1 min after (0446 UT), which was during the MI phase. At the start of the PI phase, as shown in Figure 3a, there were two prominent flow perturbations, a counterclockwise rotating flow vortex on the dawnside centered at [$X = 6Re$, $Y = -4Re$], associated with the upward PI FACs, which mapped to 70° magnetic latitude and 9 MLT, and a clockwise rotating flow vortex on the dusk centered at [$X = 7Re$, $Y = 7Re$] region, which was associated with the downward PI FACs, which mapped to 70° magnetic latitude and 15 MLT. The magnetic field lines through the center of the vortices and their footprints in the ionosphere are shown. Similarly, there were two large flow vortices at 0446 UT as shown in Figure 3b. One of them was a clockwise rotating vortex and occurred around [$X = 4Re$, $Y = -4Re$]. This vortex was responsible for the downward MI FACs, which mapped to 71° magnetic latitude and 10 MLT. Likewise, there was a vortex with an opposite sense of rotation at [$X = 4Re$, $Y = 6Re$], which was associated with upward MI FACs at 72° magnetic latitude and 16 MLT. All the flow-associated perturbations mapped back to the top of the ionosphere as FACs during the PI and MI phases. These vortices propagated toward the nightside and eventually dissipated, similar to the vortex evolution shown in Ozturk et al. (2017). The high-resolution movies showing temporal evolution of the magnetosphere and ionosphere systems after the compression are provided as supporting information. Supporting information Movie S1 shows the temporal evolution of the GM and Movie S2 shows the temporal evolution of the top of the ionosphere between 0430 and 0500 UT.

3.2. Ionospheric Response

The ionospheric responses are examined through FACs, Joule heating, ion temperature, convection profiles, and the *H* component of magnetic perturbations recorded by the virtual ground magnetometers, as shown in Figure 4. The unperturbed state at 0430 UT is shown in the first column in Figure 4a. The FAC profile on the top row shows the classic NBZ current system during northward IMF B_Z. The FAC profile was symmetric

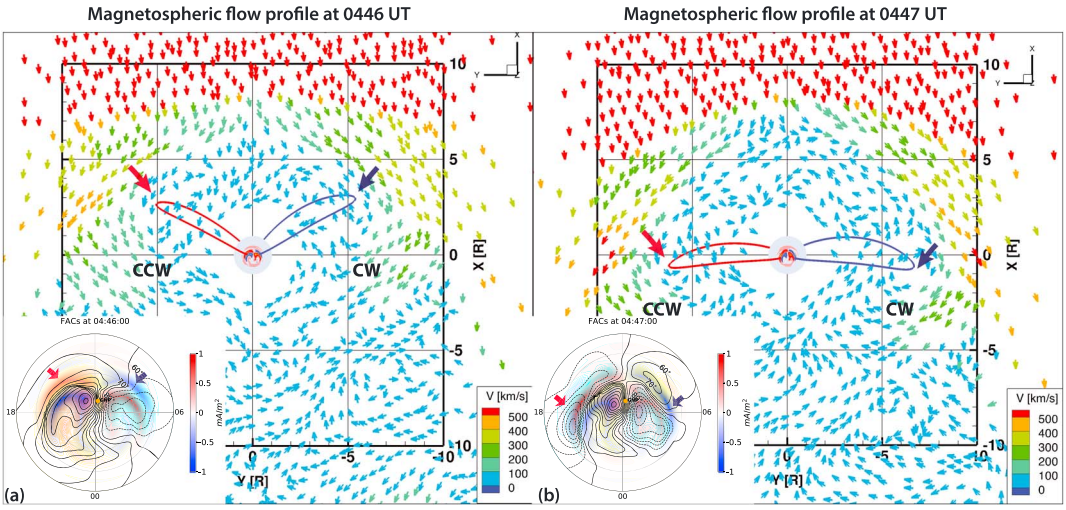

Figure 3. Equatorial magnetospheric flow profile taken at 4.45 UT (a) and 4.46 UT (b). The vectors are color coded according to their velocities. The northern FACs are shown on top of the ionosphere. The magnetic field lines centered around the flow vortices are shown and color coded (red, upward; blue, downward) depending on the FACs they map to on the top of the ionosphere. The footprints of these field lines are shown with blue and red dots on the field-aligned current profile shown in the bottom.

around noon due to the IMF B_Y being very close to zero. The second row shows the Joule heating, which was calculated from RIM using the Pedersen conductivity and electric field (Ridley et al., 2004), ignoring neutral wind. It was mostly close to zero except for the mild increments at locations where the electric potential contours were condensed. The ion temperature profile and ion convection vectors from the GITM in geographic coordinates taken at 227 km are shown in the third row. The reason for choosing this altitude was to show the effects of Joule heating and to compare the GITM results with the results shown in Schunk, Zhu, and Sojka (1994). The temperature was mostly around 1000 K, with slight enhancements to 1200 K near the higher convection flows located in the midnight region. The *H* component of the magnetic perturbations derived from the virtual ground magnetometers from BATS-R-US and RIM is shown in the fourth row, and it is shown that there was almost no perturbation occurring before the compression event.

The system responded to the compression immediately at 0445 UT, which is shown in Figure 4b. This was the PI phase of the major compression and accompanied with a perturbation FAC system (first row) that was upward on the dawnside and downward on the duskside. Correspondingly, the Joule heating (second row) increased at the locations where the electric field potential changed rapidly with the perturbation FACs. The ion convection pattern was a clockwise rotating cell in the dawn region that was associated with the upward PI FAC. Similarly, there was a counterclockwise rotating cell in the dusk region associated with the downward PI-FAC. The ion temperature profile (third row) showed significant enhancements up to 2500 K in regions of enhanced flows, mainly across the center of the polar cap and at dusk. The PI magnetic signature was negative at latitudes between 60° and 70° at dusk and positive at latitudes above 70° at dawn. In contrast, it was positive at latitudes between 60° and 70° at dawn and negative at higher latitudes at dusk.

At 0446 UT (1 min after the compression), shown in Figure 4c, a new FAC pair with opposite polarity emerged on the dayside, thus marking this interval as the start of the MI phase. The magnetospheric sources for these MI-FACs were shown in Figure 3b. The convection flows were fastest, reaching 1,000 m/s, in the region between the PI and the MI FACs. The ion temperature was also significantly enhanced in this region. The Joule heating also peaked at these locations. The convection velocities and correspondingly the ion temperatures were larger on the duskside compared to those on the dawnside. The convection cells also moved toward the nightside. Except the positive perturbation recorded around 9 MLT, there was not much change in the magnetic perturbation profile compared with the previous time.

The effects of the MI phase became clearer at 0447 UT (2 min after the compression) as shown in Figure 4d. The MI FACs moved further toward the nightside, and new convection cells emerged with opposite sense of

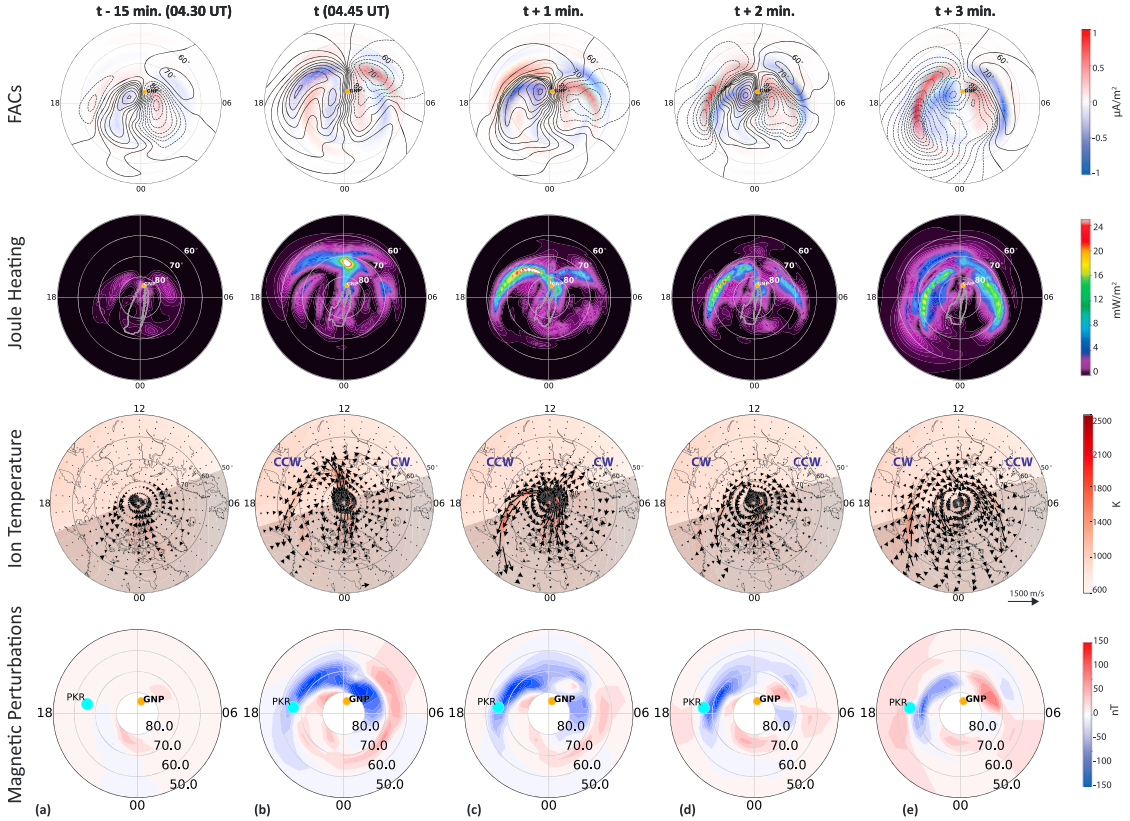

Figure 4. The field-aligned currents (first row), Joule heating profile (second row), ion temperature profile, and ion convection vectors at 227 km (third row) and the global magnetic perturbation map obtained from virtual magnetometers (fourth row) are shown at quiet time (a), 0445 UT (b), 0446 UT (c), 0447 UT (d), and 0448 UT (e). The orange dot shows the location of the geographic north pole (GNP), and the cyan dot shows the location of Poker Flat.

rotation at lower latitudes. The Joule heating profile showed a clear dawn-dusk asymmetry due to the larger scale perturbation FAC and fast convection flows on the duskside. In the bottom row, the positive magnetic perturbation in the 9 MLT region was enhanced, and the negative perturbation region in the dusk region moved toward higher latitudes and weakened.

The most pronounced effect of the MI phase can be seen in the plots for 0448 UT (3 min after the compression, 2 min into the MI phase). The MI-FACs were elongated from dayside to nightside. The convection flows corresponding to the MI FACs were stronger than those at 0447 UT, and the ion temperatures at these flow regions increased above 2000 K. The magnetic perturbation profiles at this time step were very different from the PI phase. The virtual magnetometers showed a positive perturbation at high latitudes in the dawn region and a weak negative perturbation below 70° latitude. However, in the dusk region, the magnetometers showed strong negative perturbations above ~70° latitude and weak positive perturbations below ~70° latitude.

We further explore the ionospheric and thermospheric reactions at 19 LT, where the PFISR was located during the compression. The ion and neutral temperature profiles from 100 to 600 km between 50° and 90° latitude at 19 LT (18MLT), for three different time steps, are shown in Figure 5. Over the ion and neutral temperatures, the east-west convection flow components are also shown with solid (dashed) contours for eastward (westward) flows. The unperturbed ion and neutral temperature profiles at 0430 UT are shown in Figures 5a and 5d. In general, the ion temperature (top row) increased with altitude, though there existed a perpetual high temperature region around 90° latitude, which is the region of heating near the pole in Figure 4a. The neutral temperature (bottom row) was high at two latitudes, around 50° and 90°, during the unperturbed state. Both ion and neutral temperatures responded to the start of the PI phase, that is, 0445 UT, as shown in Figures 5b and 5e. There were mild enhancements, that is, ~500 K in the ion temperature (top row) at 64°, 75°, 82°, and

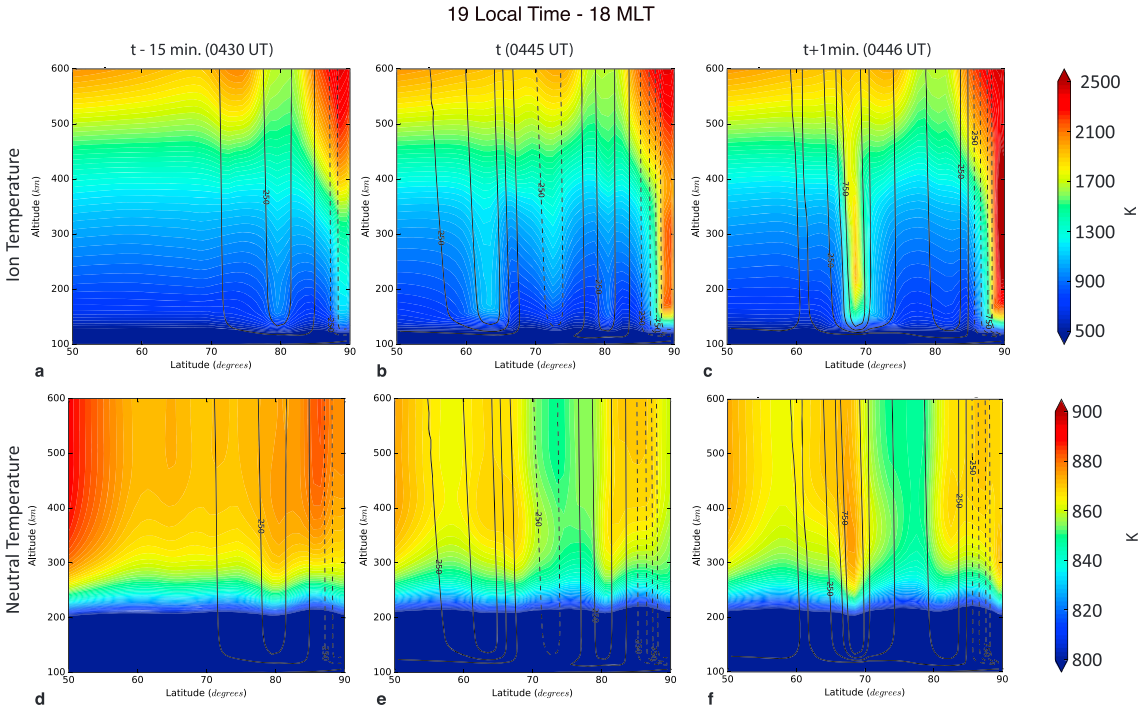

Figure 5. The vertical (100–600 km) ion (top row) and neutral (bottom row) temperature profiles at 19 LT (18 MLT) between 50° to 90° latitudes taken at (a/d) quiet time, (b/e) start of the preliminary impulse phase (0445 UT), and (c/f) start of the main impulse phase (0446 UT). Solid (dashed) lines show eastward (westward) velocity contours.

89°, corresponding to locations of enhanced Joule heating in Figure 4b. The neutral temperature shown in Figure 5e showed about a 10-K enhancement at 65° latitude. The ion temperature profile at 0446 UT, at the MI phase, showed a significant enhancement above 1000 K at 68° latitude and above 500 K at 88°. Similarly, the neutral temperature profile showed an enhancement around 20 K at the same locations, starting from 200 km. The locations of the temperature enhancements corresponded to high ion convection vectors. There were two regions where the flows were significantly enhanced. At 68° latitude, the peak was around 474 m/s at 0445 UT and 714 m/s at 0446 UT. At the pole region, the peak flow speed was around 1,026 m/s at 0445 UT and 1,786 m/s at 0446 UT. During this interval, there was a constant background cooling in the neutral and ion temperature profiles due to the region being close to the terminator, which is shown in the third row of Figure 4.

The GITM model results were extracted at 198° longitude and 68° latitude along the heating channel where the peak Joule heating was seen. This region is also very close to the PFISR location [214° longitude, 65° latitude]. The modeled altitude profiles for ion temperature, electron temperature, and density were averaged every 5 min to match the observations, which were long pulses that were integrated every 5 min to improve the signal to noise ratio. The comparisons of the modeled results with the PFISR measurements are shown in Figure 6. The averaged GITM ion temperature increased around 500 K during the compression. However, the vertical profile at 0446 UT without averaging (dotted line) shows that the peak enhancement was about 1000 K above the background temperature at the time of compression and the averaging results in an underestimation of the overall profile. The PFISR observations indicated that the peak ion temperature enhancement was about 2000 K and occurred around 200 km. The electron temperature extracted from the GITM simulations also increased around 200 K during the perturbation but then dropped to values lower than the unperturbed state after 0455 UT. Conversely, the PFISR measurements of electron temperature showed a longer and greater increase. In the bottom panels, the electron density decreased around 20% after the compression in the GITM simulations. The drop in the electron density was more drastic in the PFISR measurements, with a peak drop about 50% at 300 km. In summary, as compared to the PFISR observations, the GITM results showed that the system was disturbed, especially in the ion temperature, but not as disturbed as the observations indicated, especially in electron density and temperature.

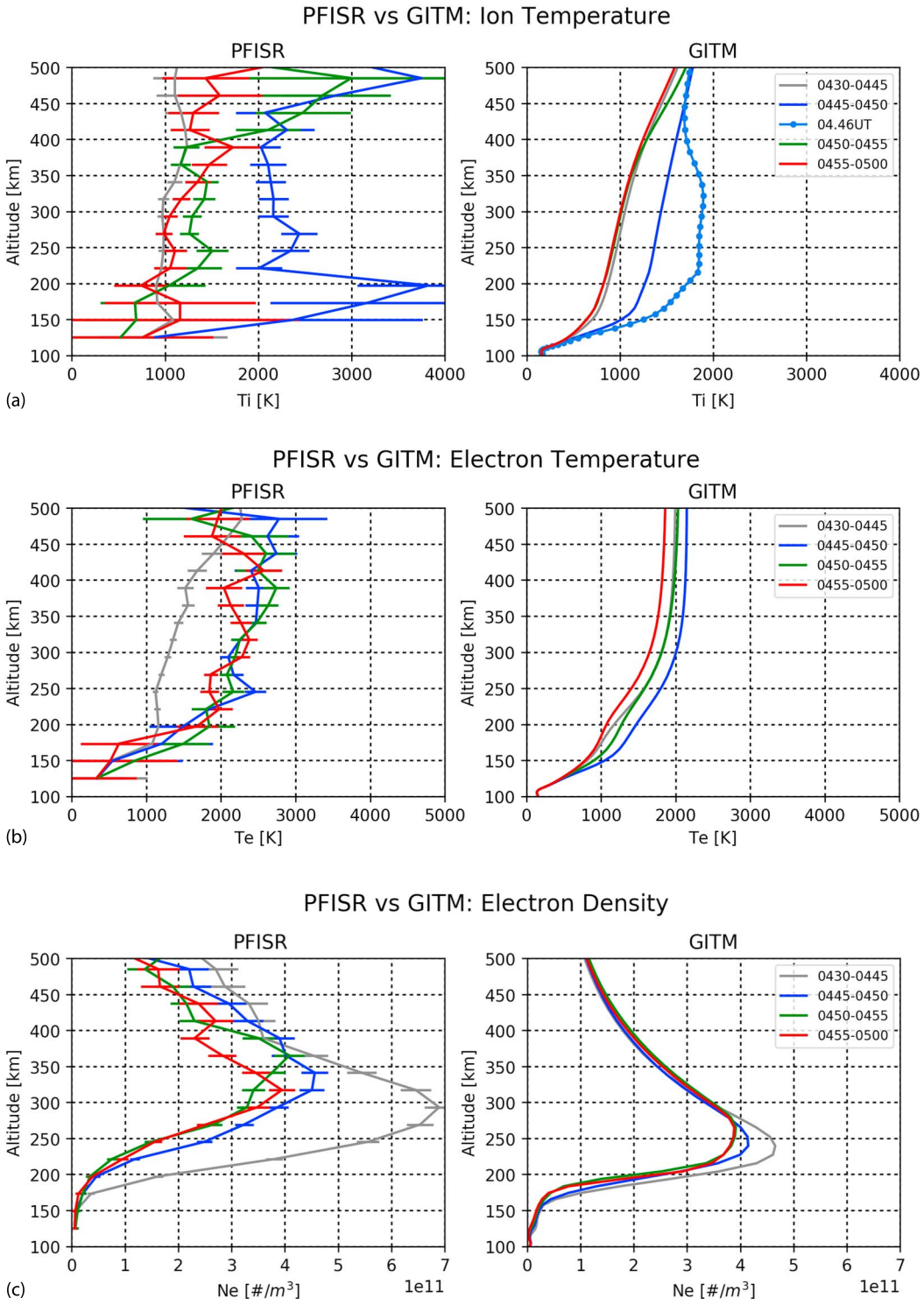

Figure 6. The vertical (100–600 km) ion temperature (a), electron temperature (b), and electron density (c) profiles taken from the PFISR observations (left) and the GITM simulation (right) at 65° latitude for 19 LT (18 MLT) are shown. The colors show the time-averaged profiles before, 0430–0445 UT (gray), during, 0445–0450 UT (blue), and after, 0450–0455 UT (green), 0455–0500 UT (red), the compression. The light blue line with dots shows the profile at 0445UT. The PFISR observations reported on the left column are adapted from Zou et al. (2017).

The modeled altitude profiles for NO^+ and O^+ densities and neutral temperature taken from the same location with the PFISR are shown in Figure 7. In the top panel, the NO^+ was initially enhanced by ~20% at ~180 km followed by a subsequent 10% decrease. The O^+ density, however, decreased by ~25% during

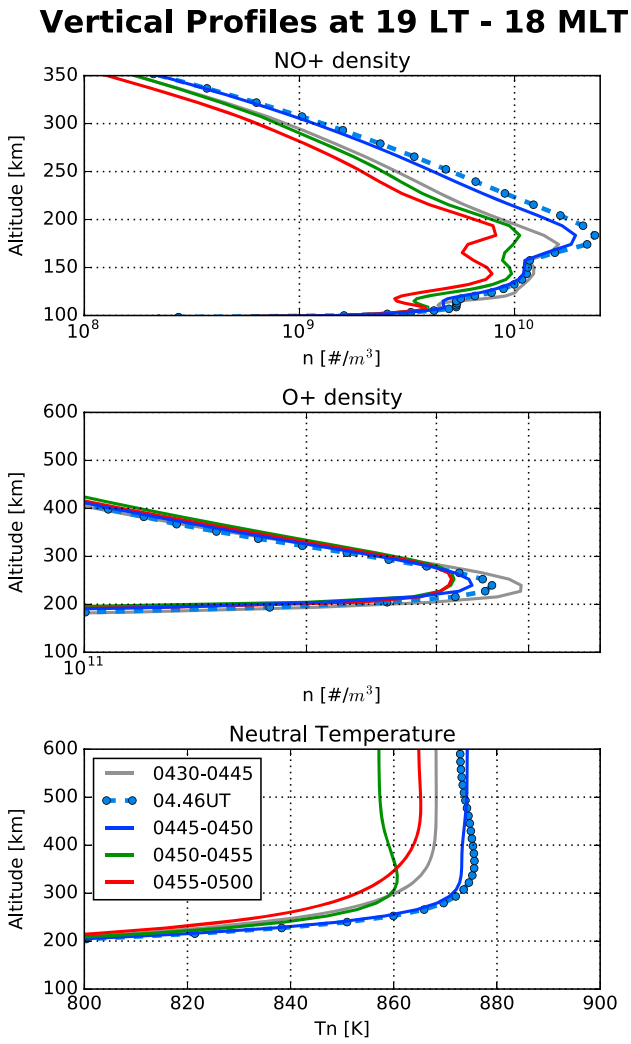

Figure 7. The vertical (100–600 km) density profiles for NO^+ (top) and O^+ (middle) and neutral temperature (bottom) are shown. The colors show the time averaged profiles before, 0430–0445 UT (gray), during, 0445–0450 UT (blue), and after, 0450–0455 UT (green), 0455–0500 UT (red), the compression. The dotted line shows the values at 0446 UT.

the compression, similar to the electron density discussed in Figure 6c. This is consistent since the O^+ is the main constituent in the *F* region of the ionosphere. In the bottom panel, the neutral temperature enhancement was clear above 200 km and demonstrated a wave-like structure, with the temperature increasing at first by approximately 10 K in the first few minutes after the PI phase, then decreasing about 10 K lower than the background temperature after 5 min, later recovering back closer to background temperature.

4. Discussions

The simulation results demonstrated that the Earth's magnetosphere was rapidly compressed as a result of the solar wind dynamic pressure enhancement, causing deformation of the magnetopause and changes in the FAC and convection flow profiles throughout the magnetosphere-ionosphere system, with the compression front propagating from the dayside to the nightside. Compression of the magnetosphere led to perturbation FACs similar to those shown by other numerical simulations (Fujita, Tanaka, Kikuchi, Fujimoto, & Itonaga, 2003; Kataoka, Fukunishi, & Lanzerotti, 2003; Ozturk et al., 2017; Slinker, Fedder, Hughes, et al., 1999; Slinker, Fedder, Emery, et al., 1999; Yu & Ridley, 2011) and reproduced based on observations (Kamide et al., 1976; Matsushita & Xu, 1982; Untiedt & Baumjohann, 1993; Weygand et al., 2011, 2012). These perturbation FACs were superimposed on the preexisting NBZ current system due to the northward IMF B_Z. The vertical ion convection patterns that formed in association with these perturbation FACs have similar physical properties to those of the TCVs (Clauer et al., 1984; Engebretson et al., 2013; Friis-Christensen et al., 1988; Glassmeier & Heppner, 1992; Hönisch & Glassmeier, 1986; Kim et al., 2015; Lanzerotti et al., 1991; Zesta et al., 2002). They formed on the dayside, near 70° latitude, and propagated toward the nightside. The BATS-R-US convection and auroral precipitation patterns were used to drive the GITM, and the corresponding results showed that the ion temperature was significantly enhanced at locations where the convection velocities were the highest and the neutral temperature was slightly increased despite the very short duration of perturbation.

The ion temperature displayed significant enhancements during the compression led TCV passage, with increases exceeding 1000 K at around 200 km altitude, consistent with observations shown by Zou et al. (2017). Likewise, the European Incoherent Scatter Svalbard radar data presented by Kim et al. (2017) during a TCV event showed that the TCV passage led to an increase in ion temperature profiles between 1000 and 3000 K with two peaks at 150 and 300 km. In addition to the observations, the simulated ion temperature profile in Schunk, Zhu, and Sojka (1994) had a single peak at 220 km with a 3000-K increase during the event. One possible reason for the difference in the ion temperature enhancements between the GITM simulations and the PFISR observations could be the disparity in the ion convection vectors, which peak around ~720 m/s in the GITM simulations but reach up to 2000 m/s in the PFISR observations as reported in Zou et al. (2017).

The variations of electron temperature are very important because of their role in the chemical processes in the I-T system as well as ambipolar diffusion. The GITM results showed a higher electron temperature during the unperturbed time and a slight enhancement of electron temperature through different altitudes. The peak enhancement of 300 K occurred at 200 km. This increase was of smaller magnitude than the radar data presented in Kim et al. (2017), which showed a significant enhancement of 1000–3000 K between 200 and 300 km, and the PFISR data from Zou et al. (2017), which showed an increase of 500–1000 K between 150

and 450 km. The enhancement of the electron temperature also appeared to last longer than the ion temperature enhancement in the PFISR observations.

The modeled ion and electron temperatures showed similar changes with the observed ones during the TCV events; however, the magnitude difference is noteworthy. The disparity between the unperturbed electron density and temperature profiles in the GITM results and the PFISR observations indicates that there is some fundamental missing process that is either not included in the GITM that can cause rapid heating of the electrons or is missed in the MHD simulation or not passed to the GITM. For example, as investigated in detail by Zhu et al. (2016) and David et al. (2011), the electron heat flux has great effects in the plasma temperature and density. In the current GITM version, the electron heat flux was added uniformly in the subauroral region mimicking the ring current effects but not in the auroral zone, which can lead to an underestimation of the plasma temperature there. In addition, the underestimated electron temperature also affects the calculation of ion temperature (Wang et al., 2006) causing lower enhancements in the ion temperature during the perturbed state.

Another reason for the low ion temperature enhancements, in addition to low auroral precipitation, could be the underestimated Joule heating (i.e., ion velocities or electron densities) in the model (Deng & Ridley, 2007; Verkhoglyadova et al., 2017; Zhu et al., 2016). In the GITM, the ion and electron temperatures are solved for in a time-accurate mode, which indicates how strongly the ion temperatures are controlled by the localized, instantaneous Joule heating. The Joule heating shown in Figure 4 was calculated from the IE module results and is higher than the heating in Verkhoglyadova et al. (2017), which used the electric potentials derived from the Weimer (2005) model to drive the GITM simulations for the same event.

When the ion temperature rises, it increases the charge exchange reaction rates, causing rapid conversion from O^+ to NO^+, followed by enhanced recombination (Schunk & Nagy, 1978). Partly due to the enhanced recombination, both the GITM results and the PFISR observations showed a decrease in electron density, with peak drops of 10% and 50% correspondingly. The simulated electron density was in general lower compared to the PFISR observations. Auroral precipitation power, which is one of the major players in the mass and momentum transfer from the magnetosphere to the I-T system, is typically underestimated in MHD models, which can cause lower electron densities and temperatures (Deng & Ridley, 2006; Slinker, Fedder, Emery, et al., 1999; Sojka et al., 1997; Wilson et al., 2006; Zhang et al., 2014).

Despite the very short duration of compression, the neutral temperature increased 5–15 K. In order to understand how the pressure-induced perturbation affects the thermosphere in detail, three sources of neutral temperature variation were picked. Equation (1) shows how the neutral temperature changes in time with these three source/loss terms (Schunk & Nagy, 2009; Zhu et al., 2016):

$$\frac{dT_n}{dt} = \frac{1}{\rho C_p}\left[\left(\sum_{\text{ions}} \frac{n_n m_n \upsilon_{ni}}{(m_i + m_n)}\left[3k(T_i - T_n) + m_i(u_i - u_n)^2\right]\right) - \frac{\partial}{\partial z}\left(\lambda_n \frac{\partial T_n}{\partial z}\right)\right] \quad (1)$$

where ρ is the mass density of the thermosphere, C_p is the specific heat under constant pressure, n_n is the neutral number density, m_i is the ion mass, m_n is the mean neutral mass, and υ_{ni} is the neutral-ion collision frequency. T_n and T_i indicate neutral and ion temperatures, respectively. The λ_n is the neutral gas thermal conductivity and calculated by AT_n^s. The A and s coefficients can be found in Schunk and Nagy (2009).

The first term on the right-hand side, $3k(T_i - T_n)$, is the ion to neutral collisional heat transfer term. The second term, $m_i(u_i - u_n)^2$, is the frictional heating term. The third term, $\partial/\partial z\,(\lambda_n\,(\partial T_n/\partial z))$, is the vertical thermal conduction term for the neutrals. To understand the sources for neutral temperature enhancement, the three heat transfer rate terms in equation (1) were investigated by using state variables extracted from the GITM simulation results, at the aforementioned location [68° latitude, 198° longitude], where the highest neutral heating occurred. Figure 8 shows the altitude profile of the three terms in equation (1) at 0446UT, when the peak heating occurred at this location. The ion to neutral collisional heat transfer and the ion-neutral frictional heating rates were very similar and peaked at ~240 km. The collisional heat transfer rate was around 0.1 K/s larger than the frictional heating term between 200 and 400 km. After the ion and neutral temperatures were enhanced near ~240 km, the temperature gradient led to enhanced vertical thermal conduction. Between 100 and 370 km, vertical heat conduction was negative, and above 370 km, it was positive. This implies that the thermosphere below 370 km was cooled by conducting heat upward and downward,

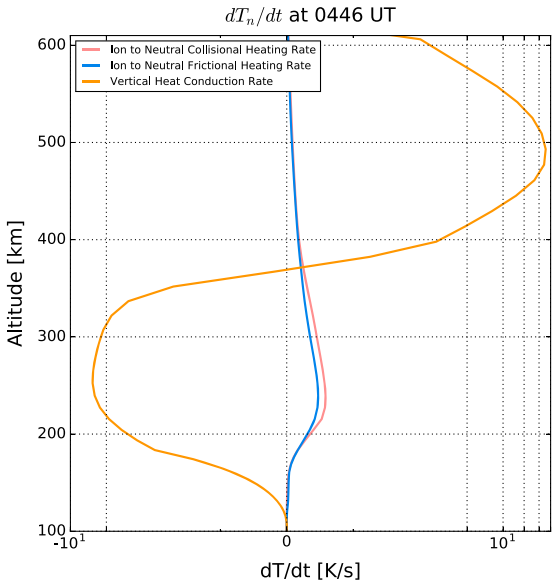

Figure 8. The altitude profile of the change in the neutral temperature per second at 0446 UT is shown. The red line shows the temperature variation due to thermal conduction from ions to neutrals, the blue line indicates the temperature variation due to frictional heating between ions and neutrals, and the orange line shows the amplitude of the heat change due to vertical heat conduction.

whereas above 370 km, the thermosphere was heated by the upward conduction from lower altitudes, since the peak in neutral temperature was around 370 km as shown in Figure 5f.

Figure 9a shows the temporal variation of the neutral and ion velocity extracted at 240 km. There were two significant peaks in neutral temperature (orange line) that shows an enhancement around 10 m/s above the background velocity. The ion velocity profile (blue line) revealed four peaks, showing up to 1,000 m/s enhancements. Both the neutral and ion velocity peaks between 0440 and 0445 UT were due to an earlier velocity enhancement in the solar wind at 0442 UT as shown in Figure 1; however, there was no evidence in the PKR data, shown in Figure 2, to prove that this was an actual enhancement. After 0445 UT, the ion velocity shows two larger peaks, which are associated with the PI and MI FACs.

Figure 9b shows the temporal evolution of the ion to neutral collisional heat transfer (red) and frictional heating (blue) rates for neutrals at 240 km altitude, where both heating terms peaked. There were four peaks in both heating rates in the plot, indicating that during the compression, both heating terms were enhanced by an order of magnitude, mainly due to the changes in the ion convection vectors associated with the PI and MI FACs. The collisional heat transfer term due to the difference between the ion and neutral temperatures was the dominant term at 240 km. At 0446 UT, the combined collisional heat transfer and frictional heating rates were more than 1 K/s, which means that the neutral temperature enhancement was around 60 K/min. From Figure 9b**,** it is clear that the thermosphere response to the solar wind dynamic pressure enhancement was immediate and caused by frictional heating and the subsequent collisional heat transfer from ions to neutrals, the latter being slightly more dominant. There was a constant cooling in the system that is not shown in Figure 9b, which was due to the decrease in the solar EUV radiation Q_{EUV} term, since the PFISR was near the terminator and the vertical conduction was constantly extracting heat from the upper thermosphere.

The computational efficiency of the empirical models makes them favorable in space weather forecasting applications; however, they cannot model the short-lived, small-scale perturbations, that is, PI and MI FACs,

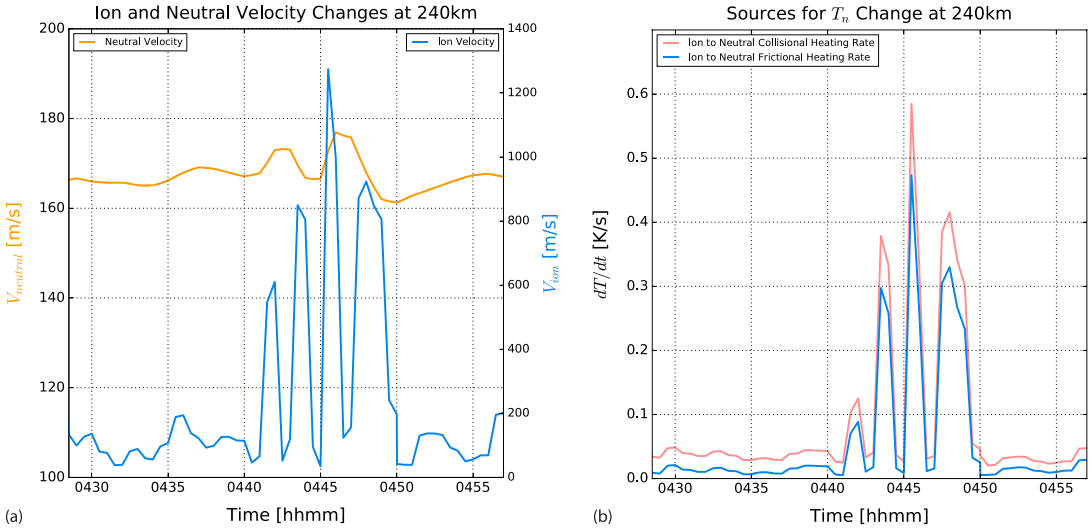

Figure 9. The temporal variations of (a) the ion and neutral velocities and (b) ion to neutral heat transfer rates per second at 240 km are shown. The orange line shows the neutral velocity while the blue line shows the ion velocity on the left. The red line shows the temperature variation due to collisional heat transfer from ions to neutrals while the blue line shows the temperature variation due to frictional heat transfer on the right.

that occur during the interaction of solar wind with the Earth's magnetosphere (Boudouridis et al., 2003; Deng & Ridley, 2007; Weimer, 2005). Various studies (Codrescu et al., 1995; Cosgrove et al., 2009) have shown that the majority of Joule heating rate comes from such transient, localized electric field perturbations making the MHD-driven electrodynamics a better tool to investigate the coupling between magnetosphere-ionosphere-thermosphere systems.

5. Summary and Conclusions

The 17 March 2015 solar wind dynamic pressure enhancement event was simulated using the BATS-R-US and the GITM in order to study the effects of the compression on the coupled magnetosphere-ionosphere-thermosphere system. The GM was significantly compressed, and two vortex pairs formed due to the propagation of the compression front. A 10-s resolution ionospheric electrodynamic potential and auroral power derived from the self-consistent global MHD model were used to drive the GITM. The scarcity of available observations since limited our ability to understand how the transient perturbations affected the I-T system globally; however, with the high-resolution drivers, we were able to investigate the effects of the compression on the compound system. The GITM simulation results provided detailed information about how the ionosphere and thermosphere were affected at different altitudes as the perturbation FACs and convection formed and propagated from the dayside to the nightside. The findings can be summarized as follows:

1. The high-latitude electric field potential and convection pattern were significantly altered during the compression. The flow speed was significantly enhanced particularly between the PI and MI FACs.
2. The ion temperature increased significantly, that is, 1000 K, in regions of high convection speed due to frictional heating between ions and neutrals. The measured ion temperature increase was much larger than the modeled increase, indicating that the Joule heating in the model was likely underestimated.
3. The ion to neutral collisional heat transfer and frictional heating rates peaked at 240 km, which corresponded to the peak electron density in the model. The collisional heat transfer and frictional heating terms contributed to the neutral temperature increase almost equally with the former contributing slightly larger. At the peak heating time, a sum of both terms led to ~60 K/min heating rate in the neutral temperature.
4. The enhancement in the ion temperature led to an increase in the atomic oxygen charge exchange rates, decreasing the net O^+ and electron density but increasing the NO^+ density.
5. The modeled perturbation in electron temperature was significantly underestimated, indicating that processes such as heat flux enhancements should be included in the magnetospheric modeling and magnetosphere-ionosphere coupling.

Acknowledgments
The authors would like to acknowledge the high-performance computing support from Yellowstone (ark:/85065/d7wd3xhc) provided by the National Center for Atmospheric Research (NCAR) Computational and Information Systems Laboratory, sponsored by the National Science Foundation, the University of Michigan Center for Space Environment Modeling and the SpacePy Team. Author Dogacan Ozturk thanks Daniel Welling and Xianzhe Jia for their useful comments. This work was supported by NSF grant AGS1203232. This research has made use of NASA's Astrophysics Data System. The Wind data used in the study are extracted from NASA/GSFC's SPDF through CDAWeb. For the ground magnetometer data, we gratefully acknowledge SuperMAG, P. I. Jesper W. Gjerloev. The simulation results discussed in this paper can be found at the University of Michigan Deep Blue Data Repository under the title "Model results for 'Modeling study of geospace system response to the solar wind dynamic pressure enhancement on March 17, 2015'," with the doi:10.7302/Z2HM56NJ.

References

Araki, T. (1977). Global structure of geomagnetic sudden commencements. *Planetary and Space Science*, *25*(4), 373–384. https://doi.org/10.1016/0032-0633(77)90053-8

Boudouridis, A., Zesta, E., Lyons, R., Anderson, P. C., & Lummerzheim, D. (2003). Effect of solar wind pressure pulses on the size and strength of the auroral oval. *Journal of Geophysical Research*, *108*(A4), 8012. https://doi.org/10.1029/2002JA009373

Cherniak, I., Zakharenkova, I., & Redmon, R. J. (2015). Dynamics of the high-latitude ionospheric irregularities during the 17 March 2015 St. Patrick's Day storm: Ground based GPS measurements. *Space Weather*, *13*, 585–597. https://doi.org/10.1002/2015SW001237

Chi, P. J., Russell, C. T., Raeder, J., Zesta, E., Yumoto, K., Kawano, H., et al. (2001). Propagation of the preliminary reverse impulse of sudden commencements to low latitudes. *Journal of Geophysical Research*, *106*, 18,857–18,864. https://doi.org/10.1029/2001JA900071

Clauer, C. R., Banks, P. M., Smith, A. Q., Jorgensen, T. S., Friis-Christensen, E., Vennerstrom, S., et al. (1984). Observation of interplanetary magnetic field and of ionospheric plasma convection in the vicinity of the dayside polar cleft. *Geophysical Research Letters*, *11*, 891–894. https://doi.org/10.1029/GL011i009p00891

Codrescu, M. V., Fuller-Rowell, T. J., & Foster, J. C. (1995). The importance of E-field variability for Joule heating in the high-latitude thermosphere. *Geophysical Research Letters*, *22*(17), 2393–2396. https://doi.org/10.1029/95GL01909

Cosgrove, R. B., Lu, G., Bahcivan, H., Matsuo, T., Heinselman, C. J., & McCready, M. A. (2009). Comparison of AMIE-modeled and Sondrestrom-measured Joule heating: A study in model resolution and electric field–conductivity correlation. *Journal of Geophysical Research*, *114*, A04316. https://doi.org/10.1029/2008JA013508

David, M., Schunk, R. W., & Sojka, J. J. (2011). The effect of downward electron heat flow and electron cooling processes in the high-latitude ionosphere. *Journal of Atmospheric and Solar - Terrestrial Physics*, *73*, 1029–1048.

Deng, Y., & Ridley, A. J. (2006). Dependence of neutral winds on convection E-field, solar EUV, and auroral particle precipitation at high latitudes. *Journal of Geophysical Research*, *111*, A09306. https://doi.org/10.1029/2005JA011368

Deng, Y., & Ridley, A. J. (2007). Possible reasons for underestimating Joule heating in global models: *E* field variability, spatial resolution, and vertical velocity. *Journal of Geophysical Research*, *112*, A09308. https://doi.org/10.1029/2006JA012006

Engebretson, M. J., Yeoman, T. K., Oksavik, K., Soraas, F., Sigernes, F., Moen, J. I., et al. (2013). Multi-instrument observations from Svalbard of a traveling convection vortex, electromagnetic ion cyclotron wave burst, and proton precipitation associated with a bow shock instability. *Journal of Geophysical Research: Space Physics*, *118*, 2975–2997. https://doi.org/10.1002/jgra.50291

Fagundes, P. R., Cardoso, F. A., Fejer, B. G., Venkatesh, K., Ribeiro, B. A. G., & Pillat, V. G. (2016). Positive and negative GPS-TEC ionospheric storm effects during the extreme space weather event of March 2015 over the Brazilian sector. *Journal of Geophysical Research: Space Physics*, *121*, 5613–5625. https://doi.org/10.1002/2015JA022214

Fok, M. C., Wolf, R. A., Spiro, R. W., & Moore, T. E. (2001). Comprehensive computational model of Earth's ring current. *Journal of Geophysical Research*, *106*, 8417–8424. https://doi.org/10.1029/2000JA000235

Foster, J. C., Holt, J. M., Musgrove, R. G., & Evans, D. S. (1986). Ionospheric convection associated with discrete levels of particle precipitation. *Geophysical Research Letters*, *13*, 656–659. https://doi.org/10.1029/GL013i007p00656

Friis-Christensen, E., McHenry, M. A., Clauer, C. R., & Vennerstrom, S. (1988). Ionospheric traveling convection vortices observed near the polar cleft: A triggered response to sudden changes in the solar wind. *Geophysical Research Letters*, *15*, 253–256. https://doi.org/10.1029/GL015i003p00253

Fujita, S., Tanaka, T., Kikuchi, T., Fujimoto, K., Hosokawa, K., & Itonaga, M. (2003). A numerical simulation of the geomagnetic sudden commencement: 1. Generation of the field-aligned current associated with the preliminary impulse. *Journal of Geophysical Research*, *108*(A12), 1416. https://doi.org/10.1029/2002JA009407

Fujita, S., Tanaka, T., Kikuchi, T., Fujimoto, K., & Itonaga, M. (2003). A numerical simulation of the geomagnetic sudden commencement: 2. Plasma processes in the main impulse. *Journal of Geophysical Research*, *108*(A12), 1417. https://doi.org/10.1029/2002JA009763

Fukushima, N. (1969). Equivalence in ground geomagnetic effect of Chapman-Vestine's and Birkeland-Alfven's current systems for polar magnetic storms. *Rep. Ionosphere Space Research Japan*, *23*, 219–227.

Glassmeier, K.-H., & Heppner, C. (1992). Traveling magnetospheric convection twin vortices: Another case study, global characteristics, and a model. *Journal of Geophysical Research*, *97*, 3977–3992. https://doi.org/10.1029/91JA02464

Glassmeier, K.-H., Hönisch, M., & Untiedt, J. (1989). Ground-based and satellite observations of traveling magnetospheric convection twin vortices. *Journal of Geophysical Research*, *94*, 2520–2528. https://doi.org/10.1029/JA094iA03p02520

Glocer, A., Fok, M., Meng, X., Toth, G., Buzulukova, N., Chen, S., & Lin, K. (2013). CRCM + BATS-R-US two-way coupling. *Journal of Geophysical Research: Space Physics*, *118*, 1635–1650. https://doi.org/10.1002/jgra.50221

Heelis, R. A., Lowell, J. K., & Spiro, R. W. (1982). A model of the high-latitude ionospheric convection pattern. *Journal of Geophysical Research*, *87*, 6339–6345. https://doi.org/10.1029/JA087iA08p06339

Hönisch, M., & Glassmeier, K.-H. (1986). Isolated transient magnetic variations in the auroral zone. *Eos Transactions American Geophysical Union*, *67*, 1163.

Huang, C. Y.-Y., Huang, Y., Su, Y.-J., Sutton, E. K., Hairston, M. R., & Coley, W. R. (2016). Ionosphere-thermosphere response to solar wind forcing during magnetic storms. *Journal of Space Weather Space Climate*, *6*. https://doi.org/10.1051/swsc/2015041

Jacobsen, K. S., & Andalsvik, Y. L. (2016). Overview of the 2015 St. Patrick's storm and its consequences for RTK and PPP positioning in Norway. *Journal of Space Weather Space Climate*, *6*, A9. https://doi.org/10.1051/swsc/2016004

Johnson, E. S., & Heelis, R. A. (2005). Characteristics of ion velocity structure at high latitudes during steady southward interplanetary magnetic field conditions. *Journal of Geophysical Research*, *110*, A12301. https://doi.org/10.1029/2005JA011130

Kamide, Y., Akasofu, S.-I., & Brekke, A. (1976). Ionospheric currents obtained from the Chatanika radar and ground magnetic perturbations at the auroral latitudes. *Planetary and Space Science*, *24*, 193–201. https://doi.org/10.1016/0032-0633(76)90016-7

Kataoka, R., Fukunishi, H., Fujita, S., Tanaka, T., & Itonaga, M. (2004). Transient response of the Earth's magnetosphere to a localized density pulse in the solar wind: Simulation of traveling convection vortices. *Journal of Geophysical Research*, *109*, A03204. https://doi.org/10.1029/2003JA010287

Kataoka, R., Fukunishi, H., & Lanzerotti, L. J. (2003). Statistical identification of solar wind origins of magnetic impulse events. *Journal of Geophysical Research*, *108*(A12), 1436. https://doi.org/10.1029/2003JA010202

Kataoka, R., Shiota, D., Kilpua, E., & Keika, K. (2015). Pileup accident hypothesis of magnetic storm on 17 March 2015. *Geophysical Research Letters*, *42*, 5155–5161. https://doi.org/10.1002/2015GL064816

Keiling, A., Angelopoulos, V., Runov, A., Weygand, J., Apatenkov, S. V., Mende, S., et al. (2009). Substorm current wedge driven by plasma flow vortices: THEMIS observations. *Journal of Geophysical Research*, *114*, A00C22. https://doi.org/10.1029/2009JA014114

Kim, H., Clauer, C. R., Engebretson, M. J., Matzka, J., Sibeck, D. G., Singer, H. J., et al. (2015). Conjugate observations of traveling convection vortices associated with transient events at the magnetopause. *Journal of Geophysical Research: Space Physics*, *120*, 2015–2035. https://doi.org/10.1002/2014JA020743

Kim, H., Lessard, M. R., Jones, S. L., Lynch, K. A., Fernandes, P. A., Aruliah, A. L., et al. (2017). Simultaneous observations of traveling convection vortices: Ionosphere-thermosphere coupling. *Journal of Geophysical Research: Space Physics*, *122*, 4943–4959. https://doi.org/10.1002/2017JA023904

Kivelson, M. G., & Southwood, D. J. (1991). Ionospheric traveling convection vortex generation by solar wind buffeting of the magnetosphere. *Journal of Geophysical Research*, *96*, 1661–1667. https://doi.org/10.1029/90JA01805

Knipp, D. J., Tobiska, W. K., & Emery, B. A. (2004). Direct and indirect thermospheric heating sources for solar cycles 21–23. *Solar Physics*, *224*(1-2), 495–505. https://doi.org/10.1007/s11207-005%206393-4

Lanzerotti, L. J., Konik, R. M., Wolfe, A., Venkatesan, D., & Maclennan, C. G. (1991). Cusp latitude magnetic impulse events: 1. Occurrence statistics. *Journal of Geophysical Research*, *96*, 14,009–14,022. https://doi.org/10.1029/91JA00567

Liu, J., Wang, W., Burns, A., Yue, X., Zhang, S., Zhang, Y., & Huang, C. (2016). Profiles of ionospheric storm-enhanced density during the 17 March 2015 great storm. *Journal of Geophysical Research: Space Physics*, *121*, 727–744. https://doi.org/10.1002/2015JA021832

Matsushita, S., & Xu, W.-Y. (1982). Equivalent ionospheric current systems representing solar daily variations of the polar geomagnetic field. *Journal of Geophysical Research*, *87*, 8241–8254. https://doi.org/10.1029/JA087iA10p08241

Motoba, T., Kikuchi, T., Okuzawa, T., & Yumoto, K. (2003). Dynamical response of the magnetosphere-ionosphere system to a solar wind dynamic pressure oscillation. *Journal of Geophysical Research*, *108*(A5), 1206. https://doi.org/10.1029/2002JA009696

Newell, P. T., Sotirelis, T., Ruohoniemi, J. M., Carbary, J. F., Liou, K., Skura, J. P., et al. (2002). OVATION: Oval variation, assessment, tracking, intensity and online nowcasting. *Annales Geophysicae*, *20*(7), 1039–1047. https://doi.org/10.5194/angeo-20-1039-2002

Nishida, A. (1964). Ionospheric screening effect and storm sudden commencement. *Journal of Geophysical Research*, *69*, 1861–1874. https://doi.org/10.1029/JZ069i009p01861

Oliveira, D. M., Zesta, E., Schuck, P. W., & Sutton, E. K. (2017). Thermosphere global time response to geomagnetic storms caused by coronal mass ejections. *Journal of Geophysical Research: Space Physics*, *122*(10), 10,762–10,782. https://doi.org/10.1002/2017JA024006

Ozturk, D. S., Zou, S., & Slavin, J. A. (2017). IMF B_y effects on ground magnetometer response to increased solar wind dynamic pressure derived from global MHD simulations. *Journal of Geophysical Research*, *122*, 5028–5042. https://doi.org/10.1002/2017JA023903

Powell, K. G. (1994). An approximate Riemann solver for magnetohydrodynamics (that works in more than one dimension), AD-280296, NASA-CR-194902, NAS 1.26:194902, ICASE 94–24, NASA. Retrieved from: ntrs.nasa.gov/search.jsp?R=19940028527

Powell, K. G., Roe, P. L., Linde, T. J., Gombosi, T. I., & De Zeeuw, D. L. (1999). A solution adaptive upwind scheme for ideal magnetohydrodynamics. *Journal of Computational Physics*, *154*(2), 284–309. https://doi.org/10.1006/jcph.1999.6299

Richmond, A. D., Ridley, E. C., & Roble, R. G. (1992). Thermosphere/ionosphere general circulation model with coupled electrodynamics. *Geophysical Research Letters*, *19*, 601–604. https://doi.org/10.1029/92GL00401

Ridley, A. J., De Zeeuw, D. L., & Rastätter, L. (2016). Rating global magnetosphere model simulations through statistical data-model comparisons. *Space Weather*, *14*, 819–834. https://doi.org/10.1002/2016SW001465

Ridley, A. J., Deng, Y., & Toth, G. (2006). The global ionosphere-thermosphere model (GITM). *Journal of Atmospheric and Solar - Terrestrial Physics*, *68*, 839–864.

Ridley, A. J., Gombosi, T. I., & De Zeeuw, D. L. (2004). Ionospheric control of the magnetospheric configuration: Conductance. *Annales Geophysicae*, *22*(2), 567–584. https://doi.org/10.5194/angeo-22-567-2004

Russell, C. T., & Ginskey, M. (1995). Sudden impulses at subauroral latitudes: Response for northward interplanetary magnetic field. *Journal of Geophysical Research*, *100*, 23,695–23,702. https://doi.org/10.1029/95JA02495

Samsonov, A. A., & Sibeck, D. G. (2013). Large-scale flow vortices following a magnetospheric sudden impulse. *Journal of Geophysical Research: Space Physics*, *118*, 3055–3064. https://doi.org/10.1002/jgra.50329

Samsonov, A. A., Sibeck, D. G., Zolotova, N. V., Biernat, H. K., Chen, S.-H., Rastaetter, L., et al. (2011). Propagation of a sudden impulse through the magnetosphere initiating magnetospheric Pc5 pulsations. *Journal of Geophysical Research*, *116*, A10216. https://doi.org/10.1029/2011JA016706

Schunk, R., & Nagy, A. (2009). *Ionospheres: Physics, plasma physics, and chemistry*. Cambridge, UK: Cambridge University Press. https://doi.org/10.1017/CBO9780511635342

Schunk, R. W., & Nagy, A. F. (1978). Electron temperatures in the *F* region of the ionosphere: Theory and observations. *Reviews of Geophysics*, *16*, 355–399. https://doi.org/10.1029/RG016i003p00355

Schunk, R. W., Zhu, L., & Sojka, J. J. (1994). Ionospheric response to traveling convection twin vortices. *Geophysical Research Letters*, *21*, 1759–1762. https://doi.org/10.1029/94GL01059

Shi, Y., Zesta, E., Connor, H. K., Su, Y.-J., Sutton, E. K., Huang, C. Y., et al. (2017). High-latitude thermosphere neutral density response to solar wind dynamic pressure enhancement. *Journal of Geophysical Research: Space Physics*, *122*, 11,559–11,578. https://doi.org/10.1002/2017JA023889

Slinker, S. P., Fedder, J. A., Emery, B. A., Baker, K. B., Lummerzheim, D., Lyon, J. G., & Rich, F. J. (1999). Comparison of global MHD simulations with AMIE simulations for the events of May 19–20, 1996. *Journal of Geophysical Research*, *104*, 28,379–28,395. https://doi.org/10.1029/1999JA900403

Slinker, S. P., Fedder, J. A., Hughes, W. J., & Lyon, J. G. (1999). Response of the ionosphere to a density pulse in the solar wind: Simulation of traveling convection vortices. *Geophysical Research Letters*, *26*, 3549–3552. https://doi.org/10.1029/1999GL010688

Smith, E. J., Slavin, J. A., Zwickl, R. D., & Bame, S. J. (1986). *Shocks and storm sudden commencements, solar wind-magnetosphere coupling*. Tokyo: Terra Scientific Publishing Company. https://doi.org/10.1007/978-94-009-4722-1_25

Sojka, J. J., Schunk, R. W., Bowline, M. D., Chen, J., Slinker, S., & Fedder, J. (1997). Driving a physical ionospheric model with a magnetospheric MHD model. *Journal of Geophysical Research*, *102*, 22,209–22,220. https://doi.org/10.1029/97JA01650

Tamao, T. (1964). The structure of three-dimensional hydromagnetic waves in a uniform cold plasma. *Journal of Geomagnetism and Geoelectricity*, *16*(2), 89–114. https://doi.org/10.5636/jgg.16.89

Tanaka, T. (2001). Interplanetary magnetic field B_y and auroral conductance effects on high latitude ionospheric convection patterns. *Journal of Geophysical Research*, *106*, 24,505–24,516. https://doi.org/10.1029/2001JA900061

Tanaka, T. (2003). Formation of magnetospheric plasma population regimes coupled with the dynamo process in the convection system. *Journal of Geophysical Research*, *108*(A8), 1315. https://doi.org/10.1029/2002JA009668

Tanaka, T. (2007). Magnetosphere-ionosphere convection as a compound system. *Space Science Reviews*, *133*(1-4), 1–72. https://doi.org/10.1007/s11214-007-9168-4

Thayer, J. P. (1998). Height-resolved Joule heating rates in the high-latitude *E* region and the influence of neutral winds. *Journal of Geophysical Research*, *103*, 471–487. https://doi.org/10.1029/97JA02536

Toth, G. (2000). The $\nabla \cdot B = 0$ constraint in shock-capturing magnetohydrodynamics codes. *Journal of Computational Physics*, *161*(2), 605–652. https://doi.org/10.1006/jcph.2000.6519

Toth, G., Sokolov, I. V., Gombosi, T. I., Chesney, D. R., Clauer, C. R., De Zeeuw, D. L., et al. (2005). Space Weather Modeling Framework: A new tool for the space science community. *Journal of Geophysical Research*, *110*, A12226. https://doi.org/10.1029/2005JA011126

Tóth, G., van der Holst, B., Sokolov, I., De Zeeuw, D., Gombosi, T., Fang, F., et al. (2012). Adaptive numerical algorithms in space weather modeling. *Journal of Computational Physics*, *231*(3), 870–903. https://doi.org/10.1016/j.jcp.2011.02.006

Untiedt, J., & Baumjohann, W. (1993). Studies of polar current systems using the IMS Scandinavian magnetometer array. *Space Science Reviews*, *63*(3–4), 245–390. https://doi.org/10.1007/BF00750770

Valladares, C. E., Alcaydé, D., Rodriguez, J. V., Ruohoniemi, J. M., & van Eyken, A. P. (1999). Observations of plasma density structures in association with the passage of traveling convection vortices and the occurrence of large plasma jets. *Annales Geophysicae*, *17*(8), 1020–1039. https://doi.org/10.1007/s00585-999-1020-6

Verkhoglyadova, O., Meng, X., Manucci, A. J., Mlynzcak, M. G., Hunt, L. A., & Lu, G. (2017). Ionosphere-thermosphere energy budgets for the ICME storms of March 2013 and 2015 estimated with GITM and observational proxies. *Space Weather*, *15*, 1102–1124. https://doi.org/10.1002/2017SW001650

Verkhoglyadova, O. P., Tsurutani, B. T., Mannucci, A. J., Mlynczak, M. G., Hunt, L. A., Paxton, L. J., & Komjathy, A. (2016). Solar wind driving of ionosphere-thermosphere responses in three storms near St. Patrick's Day in 2012, 2013, and 2015. *Journal of Geophysical Research: Space Physics*, *121*, 8900–8923. https://doi.org/10.1002/2016JA022883

Wang, W., Burns, A. G., & Killeen, T. I. (2006). A numerical study of the response of the ionospheric electron temperature to geomagnetic activity. *Geophysical Research Letters*, *111*, A11301. https://doi.org/10.1029/2006JA011698

Wang, Y., Zhang, Q., Liu, J., Shen, C., Shen, F., Yang, Z., et al. (2016). On the propagation of a geoeffective coronal mass ejection during 15–17 March 2015. *Journal of Geophysical Research: Space Physics*, *121*, 7423–7434. https://doi.org/10.1002/2016JA022924

Weimer, D. R. (1996). Flexible, IMF dependent model of high-latitude electric potentials having 'space weather' applications. *Geophysical Research Letters*, *23*, 2549–2552. https://doi.org/10.1029/96GL02255

Weimer, D. R. (2005). Improved ionospheric electrodynamic models and application to calculating Joule heating rates. *Journal of Geophysical Research*, *110*, A05306. https://doi.org/10.1029/2004JA010884

Weygand, J. M., Amm, O., Angelopoulos, V., Milan, S. E., Grocott, A., Gleisner, H., & Stolle, C. (2012). Comparison between SuperDARN flow vectors and equivalent ionospheric currents from ground magnetometer arrays. *Journal of Geophysical Research*, *117*, A05325. https://doi.org/10.1029/2011JA017407

Weygand, J. M., Amm, O., Viljanen, A., Angelopoulos, V., Murr, D., Engebretson, M. J., et al. (2011). Application and validation of the spherical elementary currents systems technique for deriving ionospheric equivalent currents with the North American and Greenland ground magnetometer arrays. *Journal of Geophysical Research*, *116*, A03305. https://doi.org/10.1029/2010JA016177

Wilson, G. R., Weimer, D. R., Wise, J. O., & Marcos, F. A. (2006). Response of the thermosphere to Joule heating and particle precipitation. *Journal of Geophysical Research*, *111*, A10314. https://doi.org/10.1029/2005JA011274

Yu, Y., & Ridley, A. J. (2009). The response of the magnetosphere-ionosphere system to a sudden dynamic pressure enhancement under southward IMF conditions. *Annales Geophysicae*, *27*(12), 4391–4407. https://doi.org/10.5194/angeo-27-4391-2009

Yu, Y., & Ridley, A. J. (2011). Understanding the response of the ionosphere-magnetosphere system to sudden solar wind density increases. *Journal of Geophysical Research*, *116*, A04210. https://doi.org/10.1029/2010JA015871

Zesta, E., Hughes, W. J., & Engebretson, M. (2002). A statistical study of traveling convection vortices using the Magnetometer Array for Cusp and Cleft Studies. *Journal of Geophysical Research*, *107*(A10), 1317. https://doi.org/10.1029/1999JA000386

Zhang, B., Lotko, W., Brambles, O., Wiltberger, M., & Lyon, J. (2014). Electron precipitation models in global magnetosphere simulations. *Journal of Geophysical Research*, *120*, 1035–1056. https://doi.org/10.1002/2014JA020615

Zhao, H. Y., Shen, X. C., Tang, B. B., Tian, A. M., Shi, Q. Q., Weygand, J. M., et al. (2015). Magnetospheric vortices and their global effect after a solar wind dynamic pressure decrease. *Journal of Geophysical Research: Space Physics*, *121*, 1071–1077. https://doi.org/10.1002/2015JA021646

Zhu, J., & Ridley, A. J. (2016). Investigating the performance of simplified neutral-ion collisional heating rate in a global IT model. *Journal of Geophysical Research: Space Physics*, *121*, 578–588. https://doi.org/10.1002/2015JA021637

Zhu, J., Ridley, A. J., & Deng, Y. (2016). Simulating electron and ion temperature in a global ionosphere thermosphere model: Validation and modeling and idealized substorm. *Journal of Atmospheric and Solar-Terrestrial Physics*, *138-139*, 243–260. https://doi.org/10.1016/j.jastp.2016.01.005

Zou, S., Ozturk, D., Varney, R., & Reimer, A. (2017). Effects of sudden commencement on the ionosphere: PFISR observations and global MHD simulation. *Geophysical Research Letters*, *44*, 3047–3058. https://doi.org/10.1002/2017GL072